Volume 1 | Number 1 | Jan 2013 | Pages 1–100

Nanoscale

www.rsc.org/nanoscale

ROYAL SOCIETY
OF CHEMISTRY

ROYAL SOCIETY
OF CHEMISTRY

www.rsc.org/nanoscale

Nanoscale

ARTICLE

Optimization of silver nanowire-based transparent electrodes: effects of density, size and thermal annealing

M. Lagrange[a], D. P. Langley[a,b,c], G. Giusti[a], C. Jimenez[a], Y. Bréchet[d], D. Bellet[a]

Silver nanowire (AgNW) networks are efficient as flexible transparent electrodes, and are cheaper to fabricate than ITO (Indium Tin Oxide). Hence they are a serious competitor as an alternative to ITO in many applications such as solar cells, OLEDs, transparent heaters. Electrical and optical properties of AgNW networks deposited on glass are investigated in this study and an efficient method to optimize them is proposed. This paper relates network density, nanowire dimensions and thermal annealing directly to the physical properties of the nanowire networks using original physical models. A fair agreement is found between experimental data and the proposed models. Moreover thermal stability of the nanowires is a key issue in thermal optimization of such networks and needs to be studied. In this work the impact of these four parameters on the networks physical properties are thoroughly investigated via in $situ$ measurements and modelling, such a method being also applicable to other metallic nanowire networks. We demonstrate that this approach enables the optimization of both optical and electrical properties through modification of the junction resistance by thermal annealing, and a suitable choice of nanowire dimensions and network density. This work reports excellent optical and electrical properties of electrodes fabricated from AgNW networks with a transmittance T = 89.2 % (at 550 nm) and a sheet resistance of R_s = 2.9 Ω/□, leading to the highest reported figure of merit.

1 Introduction

Transparent conducting materials (TCM) play an important role in many industrial applications that take advantage of their optical and electrical properties. These applications include transparent heaters,[1–3] touch screens,[4] OLEDs,[5] solar cells[6,7] and, more recently, antennas.[8] For more than 50 years, studies related to TCMs have been focusing on transparent conductive oxides (TCO), and especially indium tin oxide (ITO) which has reached process stability and maturity, ITO being extensively developed in industry and commercially viable.[9–11] However, with the growing personal consumer electronics market, some new requirements for emerging TCM have recently appeared. First, the market begins to orient towards flexible electronics in many applications domains such as lighting, energy and heating. Therefore, transparent electrodes included in these applications must be able to bend without losing their electrical properties. One of the major drawbacks of TCO being their

brittleness, research have commenced on materials with sufficient mechanical flexibility. Secondly, research focuses on minimizing materials costs by avoiding the use of indium which has a complex geo-political history surrounding its pricing and is in high demand due to ongoing use in display technology.[12] Another goal is to reduce production costs, by avoiding time-consuming and expensive fabrication processes such as those requiring vacuum deposition or high temperatures (above 300°C).

From these considerations, the development of low price transparent conducting materials suitable for flexible applications is needed.[13] The last decade has seen the emergence of several of these materials, for example graphene-based materials,[14–16] metallic nanogrids,[17] carbon nanotube networks,[18–22] metallic nanowire networks[23,24] as well as combinations of them.[25,26] Although metallic nanowire networks, and especially silver nanowire (AgNW) networks, have recently been the subject of many studies,[1,4,27–29] a better understanding of their physical properties and their optimization is lacking. Several studies in the literature have already confirmed that AgNW networks have a promising future as transparent electrodes, with optical and electrical properties comparable to those of ITO.[27,29,30] An advantage of AgNWs is their relatively simple synthesis, especially by polyol process, which is well mastered[31,32] and is suitable for large scale production. They can then be easily deposited on flexible or rigid substrates at low temperature and under atmospheric conditions, by spraying or spin coating techniques

[a.] Univ. Grenoble Alpes, LMGP, F-38000 Grenoble, France ; CNRS, LMGP, F-38000 Grenoble, France
[b.] Laboratoire de Physique des Solides, Interfaces et Nanostructures ; Département de Physique, Université de Liège, Allée du 6 Août 17, B-4000 Liège, Belgium
[c.] ARC Centre of Excellence for Advanced Molecular Imaging, Department of Chemistry and Physics, La Trobe Institute for Molecular Science, La Trobe University, Melbourne, Victoria 3086, Australia
[d.] Univ. Grenoble Alpes, SIMAP, F-38000 Grenoble, France ; CNRS, SIMAP, F-38000 Grenoble, France

See DOI: 10.1039/x0xx00000x

for example. Finally, the malleable nature of metals in general makes the AgNW suitable for flexible applications.

Regarding the optimization of the optical and electrical properties of AgNW networks, two main steps are necessary. First, finding a network density which allows a high transmission of light through the electrode coupled with a high electrical conductivity over the entire surface is primary. Typically the anticipated requirements for future transparent electrodes are a transmittance above 90 % and a sheet resistance below 100 $\Omega/\square$.[11] The actual requirements vary depending on the application, for example they are more stringent for the resistance in the solar cell industry, and can also include other parameters such as the haze factor. A tradeoff in AgNW density needs to be found in order to achieve the highest conductivity without losing the samples' transparency. The other important step is an adapted post-deposition treatment which leads to a reduction of the network electrical resistance. Several treatments have been tested on AgNW networks in literature such as mechanical pressing,[33] fast light sintering,[34] and thermal annealing.[35]

In this study, we focus on thermal annealing, which has been shown to drastically reduce the resistance of silver nanowire-based networks,[35–39] without reducing the sample transparency. The mechanisms involved during thermal annealing that affect the electrical properties of the network are detailed in this paper.

To understand the electrical behavior of metallic nanowire networks, one needs to consider percolation theory. Percolation has been already studied many times for AgNW network properties[40,41] and more generally for 2D-stick networks,[42,43] that is the most suitable model for our study. The percolation conductivity scaling law can be expressed as follows:[44]

$$\sigma \propto (n - n_c)^m \quad (1)$$

Where σ is the network electrical conductivity, n_c is the percolation threshold (or critical density) and is defined as the number of nanowires per unit area at which the network has a percolation probability of $\frac{1}{2}$, n is the network density (number of nanowires per unit area) and m is the percolation exponent. Monte Carlo simulations show that for an infinite 2D systems of percolating objects, the percolation exponent m is approximately equal to $\frac{4}{3}$.[44] The critical density n_c depends on the nanowire length, L_{NW}, and was determined from Monte Carlo simulations by Li and Zhang:[42]

$$n_c \cdot L_{NW}{}^2 = 5.637\ 26 \pm 0.000\ 02 \quad (2)$$

Equation 2 is coherent with the intuitive idea that a network composed of longer AgNW is associated with a lower critical nanowire density. Nanowire dimensions have therefore an impact on the density needed to optimize the sample: the onset of percolation in the 2D stick system is determined predominantly by the length of the wire, which therefore

governs the network sparseness at optimal density. Light scattered by the wires and the network transparency will be affected by both the diameter and length of the nanowires.

In the present work, the electrical and optical properties of randomly oriented silver nanowires deposited on glass by a cheap and rapid solution-based method, spin-coating, are explored. Here we report an original approach for investigating simultaneously the effects of AgNW dimensions, network density and thermal annealing on the physical properties. We demonstrate that such an approach enables optimization of both the optical and electrical properties leading to networks with excellent values of Haacke figure of merit.[45]

2 Results and discussion

2.1 Thermal annealing mechanisms

Post-deposition thermal annealing is known to induce a decrease in the resistance of silver nanowire networks. In order to understand the influence of network parameters such as density and nanowire dimensions on this optimization process, the different mechanisms occurring during thermal annealing need to be understood.

In the following studies, AgNWs have been spin coated on Corning glass substrates of 2.5 by 2.5 cm². The samples were then cut into four in order that several identical samples are available for experiments. Figure 1a depicts with a continuous black curve the electrical resistance behavior of a AgNW network with a density of 107 mg.m⁻², measured *in situ* during a 2°C.min⁻¹ thermal ramp rate. The AgNWs used were Ag117, see Table 1. Three main stages are identifiable on the curve. Initially, a drop of the resistance value is observable at temperature lower than 200°C. This temperature range is associated with the thermal desorption of organic residues which are present around the AgNWs and at their junctions. Included in these organic compounds are residual left from isopropanol evaporation during the deposition, performed at room temperature, and polyvinylpyrrolidone (PVP), which is an insulating polymer used as a capping agent during the nanowire synthesis.[46] PVP glass transition temperature is around 150°C. PVP might not be removed from the network below 200°C but might move from the junctions starting around 150°C, allowing a more intimate contact between AgNWs and thus a better electrical conduction of the network. SEM images didn't show any significant change in the nanowires morphology due to this stage of the process, when compared with the as deposited nanowires shown in Figure 1b.

A second resistance drop is observed in Figure 1a around 220°C, leading to the minimum resistance value, achieved at around 255°C. Figure 1c shows the network morphology when the resistance is at its minimum: some welding can be observed at the junctions. This second drop is ascribed to a local sintering of the junctions, and the minimal resistance value is achieved when

Table 1: Nanowires dimensions

the majority of junctions are sintered within the network. The image was obtained by annealing a similar sample up to 255°C at the same 2°C.min^{-1} ramp rate, and then stop the heating to let the sample cool back to room temperature (red dashed curve in Figure 1a). This experiment allowed SEM investigation of the network morphology at this stage of the process and demonstrates the reproducibility of thermal annealing effects for similar samples.

It is worth noticing that the red dashed curve during the cooling shows that the electrical resistance of the network presents a linear dependence with temperature. This phenomenon can be modeled by a linear approximation of the temperature-dependence of electrical resistivity as written in Equation 3 which relates the increase of the electrical resistance with temperature due to phonon-induced scattering.

$$\rho(T_0 + \Delta T) = \rho_0(T_0) \cdot (1 + \beta_R \cdot \Delta T) \quad (3)$$

β_R is the temperature coefficient of resistivity and is equal to 3.8 x 10^{-3} K^{-1} for bulk silver.[47] Bid et al.[48] observed a similar value for individual and very pure AgNW. In the present work, β_R was found from Figure 1a to be around 2.2 ± 0.1 x 10^{-3} K^{-1}. The difference between bulk silver and AgNW network might arise from the presence of junctions between AgNWs which could behave differently, as well as defects such as grain boundaries present in commercial AgNWs.

The electrical resistance eventually increases sharply above 275°C, as shown in Figure 1a. This is associated with a morphological instability of the AgNWs themselves. SEM observations in Figure 1d confirm that the AgNWs are degraded at high temperature and eventually spheroidize, as also discussed by Langley et al.[35] The network loses its percolative nature since the electrical conducting pathways have been degraded. The origin of the spheroidization is called Rayleigh-Plateau instability and has already been observed on other metallic nanowires, for example by Karim et al. on gold nanowires.[49] This phenomenon appears as atomic diffusion is enhanced when temperature increases, the nanowires then tend to decrease their surface energy and eventually adopt a semi-spherical morphology.

The influence of thermal annealing ramps can be summarized as follows: initially, as the temperature increases, organic molecules adsorbed on the surface of the wires are removed, improving junction contact. At higher temperatures, atomic diffusion driven by surface energy minimization allows sintering at nanowire junctions, improving the electrical properties. At higher temperature the same driving force, reduction of total surface energy, leads to the transformation of the nanowires into a succession of droplets, degrading the percolating pathways. This deteriorates the conductive nature of the AgNW network, and leads to the divergence of the

electrical resistance. Transmittance does not show any change

	Ag26	Ag45	Ag55	Ag117	Ag138
Average diameter (nm)	26	45	55	117	138
Average length (µm)	20.4	13.6	7.6	42.9	32.0

with annealing treatment, at least before spheroidization.

The electrical behavior of silver nanowire networks during a ramp shows clearly that an optimum resistance can be reached, when nearly all nanowire junctions are welded, but before
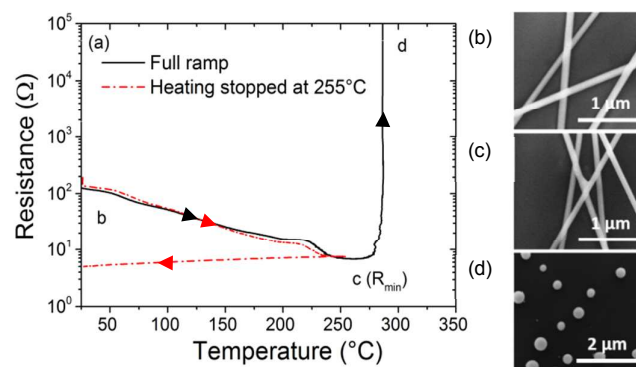

Figure 1: a) Variation of the electrical resistance of a Ag117-based network with an areal mass density of 107 mg.m^{-2}, during a thermal annealing in air running from room temperature to 500°C with a heating ramp rate of 2°C.min^{-1} (black solid line). Another similar specimen was submitted to the same annealing but only up to 255°C, temperature at which the minimum resistance is reached for this sample, and was cooled down afterwards (red dashed curve). SEM images show the morphology changes of the network at different stages indicated in the graph by letters b, c and d: b) as deposited c) optimum resistance (255°C) d) after spheroidization (500°C).

spheroidization dominates the process. The optimized conduction could be obtained either by a ramped annealing stopped at the optimized temperature as discussed in the present paper (red dashed curve in Figure 1a) or by an annealing at a constant but lower temperature for a specific duration (see the work of Giusti et al.[36]), these parameters depend on the nanowire morphology.

2.2 Network density dependence of thermal annealing effects

In order to achieve the best balance between optical and electrical properties, suitable for their use as transparent electrodes, an optimum density needs to be determined for different nanowire geometries. Samples fabricated from five different types of nanowires (see Table 1) were thermally annealed with the results displayed in Figure 2 a-e. Several densities were investigated for each type of nanowire. Annealing treatments were performed in air from room temperature to 500°C with a 2°C.min^{-1} ramp rate. The network densities displayed in Figure 2 a-e correspond to samples with optical transmittances at 550 nm close to 78-82% (black curves), 86-89% (red curves), 91-92% (blue curves), 93-94% (green curves) and 96% (magenta curves), once the substrate contribution to the transmittance is removed.

Although similar observations can be noted when compared with Figure 1, Figure 2 a-e shows that the impact of thermal annealing is more significant on low density networks, as resistances can decrease by 3 orders of magnitude or more. For example the sample with transmittance 90.9% of Ag55 series or with transmittance 92.6% of Ag138 series resistances (blue and green curves, respectively) decreased from 10^4 to 13.9 Ω and from 2.10^4 to 17.8 Ω, respectively. Some samples with low network density (for instance sample with transmittance 96.2% of Ag45, magenta curve) seem not to percolate at the beginning of the treatment (R > 10^5 Ω) because of their high junction resistance, but then resistance value starts decreasing as efficient electrical pathways are created due to the isopropanol desorption, PVP removal and local sintering. For less transparent samples, the thermal annealing induces a visible resistance decrease only above 120°C, as for the samples with transmittance 89.2% of Ag117 (red curve) and with transmittance 80.3% of Ag26 (black curve). It can be explained by considering that, as these samples are associated with high AgNW densities, there are statistically more chances to find efficient conducting pathways on the sample before annealing.

Individual creations of conducting pathways are visible for low density networks made from large-diameter nanowires, where some steep steps in resistance are identifiable at low temperature (see the black rectangle in Figure 2e). This phenomenon can be simply modeled by considering the creation of efficient conduction pathways as resistances in parallel. This geometrical quantized percolation appears when resistances corresponding to junctions between nanowires decrease during thermal annealing.[35] Since this decrease is a random process, some junctions become efficient while other still exhibit very large resistance. When a new efficient percolating pathway is created across the sample, a sudden electrical resistance drop is observed. Later on during the annealing process, a state is achieved where the number of efficient junctions is large enough to then lead to a continuous decrease of the resistance. This phenomenon is not the main topic of this article but more information has been given by Langley *et al.*[35]

2.3 Nanowires dimensions dependence of thermal annealing effects

Figure 2 shows that the *in situ* electrical resistance behavior of AgNW networks is slightly different depending on the type of nanowires used. Both the spheroidization temperature (T_{sph}) and the temperature at which minimum resistance was observed for each sample (T_{Rmin}) increase with nanowire diameter. T_{sph} was considered to occur when the network resistance was R > 10^6 Ω, after the minimum resistance was achieved.

As shown in detail in Figure 3, the characteristic temperatures cited above depend on nanowire diameter. Note that the experimental T_{Rmin} and T_{sph} reported in Figure 3 are taken from data shown in Figure 2 a-e and averaged over each density series. The error bars represent one standard deviation of the experimental values from the different samples studied, for each type of AgNW. The observed trend in Figure 3 can be

explained by surface effects enhancement which occurs for small AgNW diameters. By analogy with cluster physics,[50] many physical or chemical properties $G(r)$ vary with cluster size r, and generally follow the scaling law:

$$G(r) = G(\infty) \cdot (1 - \frac{l_c}{r}) \quad (4a)$$

Where $G(\infty)$ is the value of the specific property G associated with large r values (*i.e.* bulk properties), and l_c is a characteristic length.

Equation 4a is often called Thomson's equation.[51] The best known illustration of effects described by Equation 4a for nanoparticles or clusters is the dramatic deviation of melting
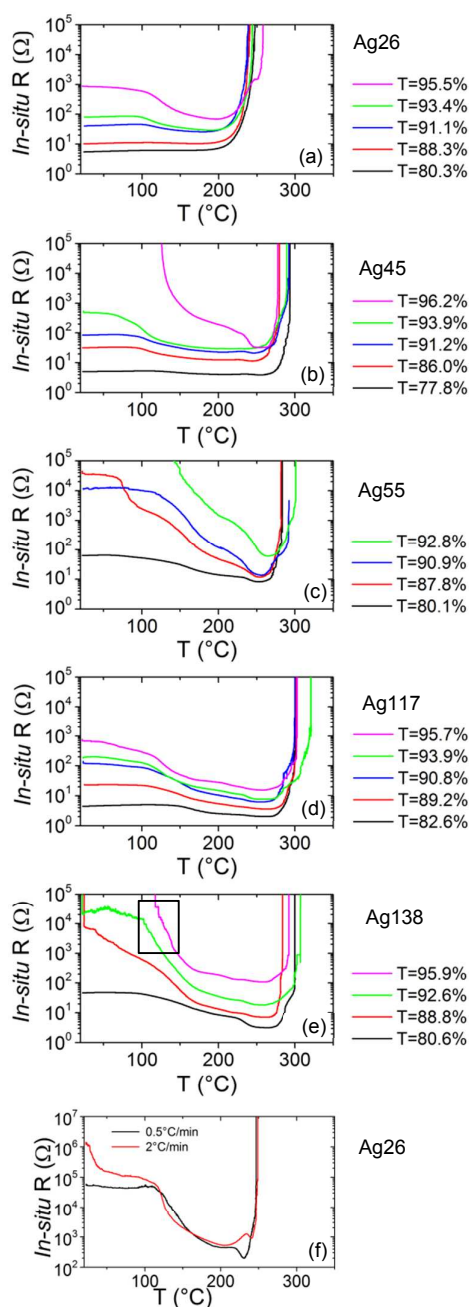
Figure 2: a)-e) In situ resistance behavior of AgNW-based transparent electrodes, during a thermal annealing in air running from room temperature with a heating ramp rate of 2°C.min^{-1}. The samples of each series have transmittances values (at 550 nm, without substrate contribution) close to 78-82% (black curves), 86-89% (red curves), 91-92% (blue curves), 93-94% (green curves) and 96% (magenta curves). The black square in e) shows the steep steps in resistance corresponding to the individual creation of percolation pathways. Note that all electrical resistance and temperature scales are identical from a) to e) for the sake of comparison. f) Comparison between in situ resistance behaviors of a Ag26-based sample with a transmittance at 550 nm of 97.3% during a 2°C.min^{-1} and a 0.5°C.min^{-1} thermal ramp rates.

$$T_m(r) = T_m(\infty) \cdot \left(1 - \frac{2 \cdot V_m^S \cdot \gamma_s}{L \cdot r}\right) \qquad (4b)$$

where, in the case of silver, V_m^S is the bulk Ag molar volume (10.3 cm^3.mol^{-1}), γ_s the free surface energy and L the molar latent heat of melting (11.3 kJ.mol^{-1}).[47]

Equation 4b is coherent with the fact that nanomaterials are able to undergo sintering at much lower temperatures compared to their bulk material[52] as also illustrated in the present work. Equation 4a can be used to describe the dependence of both T_{Rmin} and T_{sph} versus AgNW diameter as depicted in Figure 3 by the dashed lines. Physical estimation of l_c can be considered by comparing Equation 4a and Equation 4b. γ_s value depends on crystallographic orientations and generally ranges between 1 and 1.5 J.m^{-2} for bulk silver.[53] This would lead to a value of l_c between 1.8 and 2.7 nm. However, physical values often differ between bulk- and nano-materials. Indeed surface energy of (100) facets in silver nanowires has been found by Zhang *et al.*[54] to be 0.41 eV.atom^{-1} (*i.e.* 0.78 J.m^{-2}), resulting in a theoretical value of l_c equals to 1.42 nm.

To validate the model, the insert in Figure 3 shows the observed temperatures T_{sph} and T_{Rmin} as a function of the inverse of the nanowire diameter. A linear dependence is clearly observable in agreement with Equation 4b. Linear fitting of the data with the l_c value of 1.42 nm is well adapted for the inset but also to fit the main graph in Figure 3, showing good agreement between experimental and calculated values. The comparison between the theoretical Equation 4b and the observed characteristic temperature dependence versus AgNW diameter exhibits good
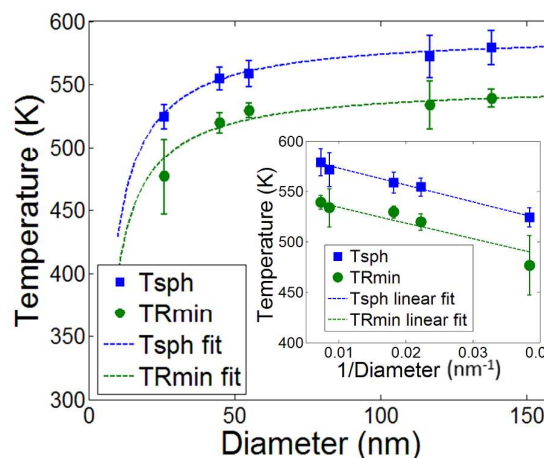
Figure 3: Temperature of spheroidization and temperature of minimum resistance (both observed during a thermal annealing with 2°C.min^{-1} ramp rate) depending on nanowire diameter. Each point is an average of the data from samples with various densities and error bars correspond to one standard deviation. The dashed lines correspond to Equation 4a associated to the Gibbs-Thomson model, with l_c=1.42 nm. The insert shows the linear dependence of both temperatures with the inverse of the diameter, according to Equation 4b.

point from the bulk since the melting point change is inversely proportional to the particle radius r, leading to:

agreement although the geometry of our system is different from the theoretical one. More precisely, clusters are generally spherical while AgNWs have a long cylindrical shape.

Moreover the presence of the substrate associated with the fivefold symmetry of the AgNWs complicates the interpretation since it has been observed that these features influence the thermal stability of metallic nanowires.[55] Finally for very small AgNW diameter, the values of the physical quantities such as the molar latent heat of melting L could differ from the bulk values.[56] In conclusion although the detailed mechanisms governing the modifications of the physical properties of AgNWs during thermal annealing are complex, a simple analysis based on the Gibbs-Thomson equation, leading to Equation 4b, describes fairly well the experimental observations. It might appear questionable that the same l_c value has been used for both T_{sph} and T_{Rmin}. However these processes, spheroidization and local sintering, respectively, are strongly dependent upon atomic diffusion and have similar driving force: surface energy reduction.

Equation 4b could be used as a guideline for the purpose of finding the most suitable thermal process in terms of temperature to improve the sample conductivity. Figure 3 clearly indicates that the lower the AgNW diameter, the lower the temperature at which the thermal process should be performed as the temperature stability is more critical. However the temperature needs to be sufficiently high for organic desorption.

2.4 Nanowire dimensions dependence of thermal annealing kinetics

In addition to the dependence of the characteristic temperatures on AgNW dimensions, the general behavior of resistance during thermal annealing is also different depending on the type of nanowires. As explained above, AgNW associated with low diameters spheroidize at lower temperature. However, the different stages corresponding to the thermally activated mechanisms of conductivity improvement through junctions, while clearly visible for larger AgNW, are not at all visible in the resistance curves of Ag26. For example the local plateau followed by a second reduction step corresponding to junction sintering is not visible in Figure 2a. It has however been observed that when decreasing the ramp rate to 0.5°C.min^{-1}, the steps were then observable, as shown in Figure 2f. This change in behavior shows that depending on the diameter, the kinetics of the thermal process is different. Indeed for a smaller diameter, the process occurring during heating has faster kinetics since surface diffusion is exacerbated due to the increase of surface over volume ratio. The Ag26 samples did not exhibit all the thermal mechanisms allowing resistance reduction with a ramp rate of 2°C.min^{-1}; this might explain their poor electrical properties. They indeed could not achieve the expected minimum resistance value for the ramp rate used because spheroidization already dominated the process at the temperature at which, normally, sintering occurrs on samples made with larger-diameter nanowires. With a thermal ramp rate of 0.5°C.min^{-1} the different stages pictured in Figure 1a were observable for Ag26 and the minimum resistance was found to be lower (see Figure 2f). For example, samples with transmittances equals to 95.5% and 97.3% had minimum

resistances of 65 and 350 Ω, respectively, with a ramp rate of 2°C.min^{-1}, and minimum resistances of 36 and 127 Ω, respectively, with a 0.5°C.min^{-1} ramp rate.

These results show the influence of AgNW dimensions on kinetics and more generally the importance of kinetics in the process of thermal annealing.

2.5 Percolation, electrical performances depending on density and nanowire dimensions

The impact of thermal annealing on electrical properties has been discussed for networks with different densities made from nanowires with different dimensions. Let us now consider and model their impact on the electrical properties, in particular within the framework of percolation theory.

To analyze experimentally the validity of Equation 1 for percolating AgNW networks, it is necessary to compare the experimental and theoretical values of the critical density n_c, the theoretical one being calculated from Equation 2. To calculate the experimental n_c value, samples with densities close to the percolation threshold were observed for each type of nanowires. Instead of nanowire density (n), the areal mass density (amd) defined as the density n times the average mass of one single AgNW is considered. amd is used instead of n since it takes into account the AgNW experimental length and diameter distributions. As briefly described in the experimental section, amd values were obtained from SEM image analysis. An example of analyses of data corresponding to Ag117 nanowires is displayed in Figure 4a. The open blue dots correspond to resistances values obtained from percolating samples while the open red rectangles correspond to non-percolating samples, with resistances above the setup detection limit, *i.e.* $> 10^7$ Ω. The experimental ranges of critical mass densities amd_c^{exp} were obtained from data like those presented in Figure 4a, by considering the lowest density at which the samples percolate (amd_2, blue dots), and the highest density at which the samples do not percolate (amd_1, red squares). The theoretical amd_c values were calculated by using Equation 2, considering only the average AgNW length. The amd_c values versus the theoretical amd_c are reported in Figure 4b, for each nanowire geometry.

While we can observe a qualitative agreement, especially for the three smallest values of amd_c, experimental results can deviate from theory. This deviation can be easily explained. First, in the simulated case from which Equation 2 was determined, all the nanowires have identical length, zero diameter and are also perfectly straight. In reality experimental wires have a distribution of lengths and diameters and can also be curved. Second, in the simulations wires are placed with a completely uniform isotropic angular distribution whereas in the case of spin coating there is a slight angular anisotropy resulting from the radial alignment of AgNWs during deposition that can induce an increase of the percolation threshold. Moreover some structural defects, such as grain boundaries, should also have a detrimental impact on the network electrical properties. These arguments suggest that the experimental n_c, and hence amd_c^{exp} values, should be larger

than the theoretical ones, as observed in Figure 4b. Moreover from a more fundamental point of view, the role of fluctuations near a critical point in any phase transition is important and are not considered by classical theory (Landau theory)[57] such as percolation theory described by Equation 2, and therefore only a qualitative agreement can be expected.

As shown in Equation 1 the network conductivity is dependent on network density n and n_c, the latter being determined from Equation 2. However Equation 2 only considers the nanowire length for the calculation of the critical density; in reality the nanowire diameter will also play a role regarding both transparency and conductivity. The impact of nanowire diameter on the conductivity is secondary to the formation of percolating pathways meaning that the electrical behavior is dominated by the wire length except when wire diameter approaches the mean free path of electrons in the material. In that case, the proportion
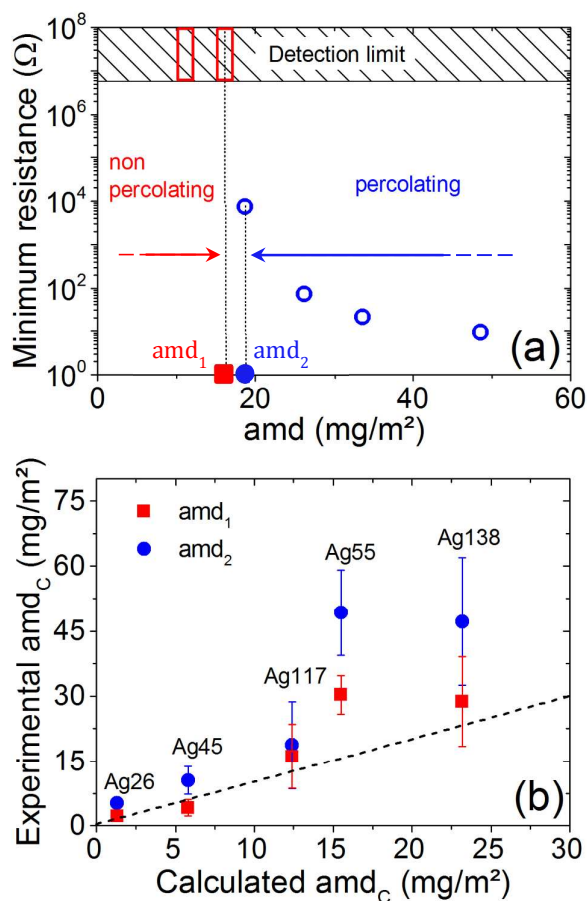

Figure 4: a) Display of minimum resistances measured during 2°C.min^{-1} thermal annealing against areal mass density, of samples made of Ag117 with densities around amd_c to find the experimental critical density delimited by the first percolating (blue) sample and the last non-percolating (red) sample. b) Comparison between experimental and calculated amd_c values for the five types of AgNW investigated in the present paper. The blue symbols amd_2 correspond to the lowest density of percolating AgNW networks, the red ones amd_1 are associated to the highest density of non-percolating AgNW networks. The dashed line is associated with a slope unity, showing a

rather good agreement between experimental and theoretical amd_c values calculated from Equation 2.

of electrons undergoing surface scattering increases, leading to an increase of the AgNW resistivity[48]. However on the optical point of view, a low diameter is beneficial to increase the transmittance and decrease the proportion of photons scattered by the nanowire,[58,59] in agreement with experimental data discussed below.

In the introduction, Equations 1 and 2 show that the network electrical conductivity σ (or resistivity ρ) depends on nanowire density and on nanowires length. But there should also be a linear dependence of ρ with the electrical resistivity of an individual AgNW, written ρ_{NW}^{Ag} .

Therefore, from Equation 1, one can deduce that the network electrical resistance R should follow this dependence:

$$R \propto \rho_{NW}^{Ag} \cdot (n - n_c)^{-\gamma} \qquad (5)$$

Bid *et al.* formulated a relation between the resistivity of a nanowire and its diameter which they confirmed experimentally.[48] They stated that the electrical resistivity of an individual AgNW can be written as follows:

$$\rho_{NW}^{Ag} = \rho_{bulk}^{Ag} \cdot \left(1 + \frac{\Lambda}{2 \cdot D_{NW}}\right) \qquad (6)$$

with ρ_{bulk}^{Ag} the resistivity of bulk silver, D_{NW} the nanowire diameter and Λ the bulk Ag mean free path. Equations 1, 2, 5 and 6 can be used to write an expression of the network resistance depending on nanowire diameter, length and network density. The network should be considered in series with an instrumental set-up resistance, R_0. This leads to:

$$R(amd, D_{NW}, L_{NW}) = R_0 + C \cdot \rho_{bulk}^{Ag} \cdot \left(1 + \frac{\Lambda}{2 \cdot D_{NW}}\right) \cdot \left(amd - \frac{5.64 \cdot d_{bulk}^{Ag} \cdot \pi \cdot D_{NW}^2}{4 \cdot L_{NW}}\right)^{-\gamma} \quad (7)$$

where R_0 was measured experimentally to be 0.8 Ω, AgNW length is noted as L_{NW}, d_{bulk}^{Ag} is the mass density of bulk silver and amd is the sample areal mass density that can be expressed in mg.m^{-2}. C is unknown and is of the same order of magnitude for all the nanowires types. However it can vary slightly and should at least be dependent upon the network geometry that was kept fixed for all experiments in the present work. It could also depend on the nanowires dimensions distribution, which varies with the nanowire type, and on the AgNW crystalline quality. Note that this model neglects the junctions resistance and therefore is valid only when the minimum resistance is reached, as the contact area between adjacent nanowires is optimized.

Minimum experimental resistances observed during the 2°C.min^{-1} thermal annealing for the different types of AgNW at

various *amd* have been measured *in situ*. Eventually, these values have been extrapolated to room temperature values by using Equation 3, as if the samples had been cooled back to room temperature, like the red dashed curve in Figure 1. These room temperature extrapolated values of minimum resistance have been plotted for all samples in Figure 5a.

All the data can be fitted with Equation 7, and those for Ag117 and Ag138 are reported on Figure 5b as examples. A fairly good agreement is observed by considering γ =1.33, that is the theoretical value of the percolation exponent for 2D infinite systems, and C=7.10^{10} mg$^{4/3}$.m$^{-11/3}$ for Ag117 and C=11.10^{10} mg$^{4/3}$.m$^{-11/3}$ for Ag138. It is worth noticing that Equation 7 was used with only one fitting parameter, C, while all the other parameters (AgNW diameter and length, network density and R_0) can be experimentally measured or are known. The slight scattering of the experimental data arises from the probabilistic nature of sparse networks. As explained above, Equation 7 considers that AgNW networks are perfect while defects such as grain boundaries along AgNWs, diameter and length distributions or AgNW curvature, suggest that one should
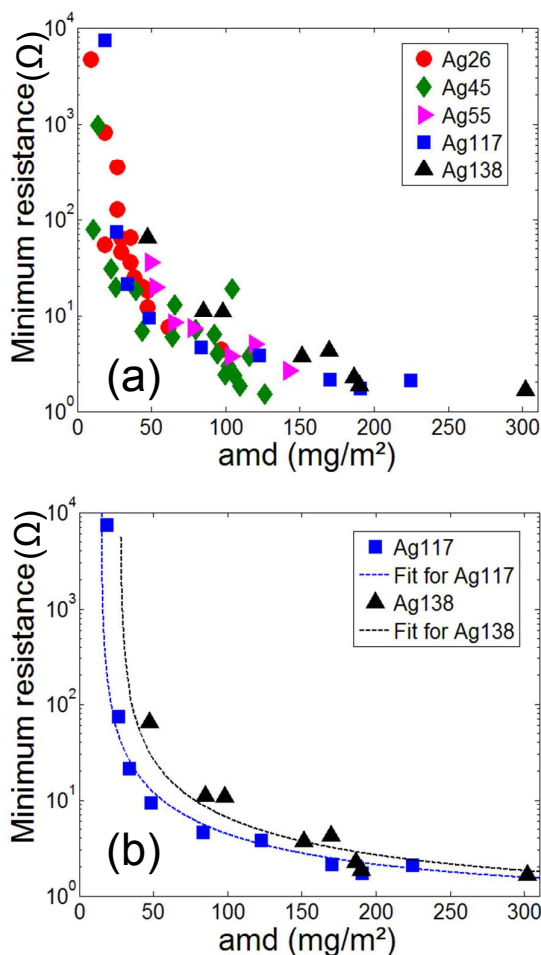

Figure 5: a) Minimum experimental electrical resistance values achieved during a 2°C.min^{-1} ramp annealing of networks made from different nanowire types and different areal mass densities. The resistance values correspond to minimum resistance

extrapolated at room temperature by using Equation 3. b) Same experimental data for Ag117 and Ag138 along with the fitted values calculated with Equation 7.

consider Equation 7 as a minimum limit for the network electrical resistance. As seen previously, density is a key parameter ruling the sample conductivity, as well as nanowire dimensions which are critical and lead to different electrical properties. But these parameters also have an impact on the optical properties.[60]

2.6 Optical performances and dependence on density

To obtain both high optical transparency and high electrical conductivity, a balance must be found, considering that conductivity increases with density while transparency decreases. The optical transmittance of a homogeneous layer decreases as it becomes thicker. Figure 6a shows that this is also valid for non-continuous films such as silver nanowire networks, as increasing the amount of nanowires lowers the total transmittance. Besides, for all NW types, a linear dependence between transmittance and areal mass density is clearly observable. Simple considerations based on shadowing effects have already been reported in the literature where transparency was supposed to decrease linearly with the increase of the area coverage of nanowires.[60,61] One can consider a slightly more sophisticated approach as follows. If one notes f_{NW} the fraction of the substrate surface covered by nanowires, the AgNW network total transmittance T_{opt} can then be written as the sum of the two following contributions associated to the covered and non-covered parts of the substrate:

$$T_{opt} = f_{NW} \cdot \left(1 - R_{opt}^{Sub}\right) \cdot T_{opt}^{Sub} \cdot \left(1 - R_{opt}^{AgNW}\right) \cdot T_{opt}^{AgNW} + \left(1 - f_{NW}\right) \cdot \left(1 - R_{opt}^{Sub}\right) \cdot T_{opt}^{Sub} \qquad (8)$$

where R_{opt}^{AgNW} and T_{opt}^{AgNW} are the averaged optical reflection and transmittance, respectively, associated with a single AgNW, while R_{opt}^{Sub} and T_{opt}^{Sub} are the averaged optical reflection and transmittance, respectively, associated with the bare glass substrate. The average optical transmittance of a single AgNW, assumed to be a cylinder of diameter D_{NW}, can be estimated using the following integral:

$$T_{opt}^{AgNW} = \int_0^1 \exp(-\alpha \cdot D_{NW} \cdot \sqrt{1 - x^2}) \cdot dx \qquad (9)$$

where α is the optical absorption coefficient associated with AgNW.

Equation 8 leads to the following expression of T_{opt}:

$$T_{opt} = \left(1 - R_{opt}^{Sub}\right) \cdot T_{opt}^{Sub} \cdot \left[1 - \frac{4 \cdot amd}{\pi \cdot d^{Ag} \cdot D_{NW}} \cdot \left(1 - \left(1 - R_{opt}^{AgNW}\right) \cdot T_{opt}^{AgNW}\right)\right] \quad (10a)$$

$$T_{opt} = T_{opt}^0 \cdot (1 - \beta \cdot amd) \quad (10b)$$

where amd is the network areal mass density (in mg.m^{-2}), d^{Ag} is the density of bulk silver, D_{NW} the AgNW diameter. T_{opt}^0 refers to the optical transmittance of the substrate and is equal to:

$$T_{opt}^0 = (1 - R_{opt}^{Sub}) \cdot T_{opt}^{Sub} \quad (10c)$$

Therefore the transmittance of the network (equal to T_{opt}/T_{opt}^0) can be written as:

$$T_{opt}^{net} = 1 - \beta \cdot amd \quad (11)$$

Equation 11 then describes a linear dependence of T_{opt}^{net} measured at 550 nm versus amd in agreement with data reported on Figure 6a for the considered range of amd. The slope β of the curve T_{opt}^{net} versus amd is equal to:

$$\beta = \frac{4}{\pi \cdot d^{Ag} \cdot D_{NW}} \cdot (1 - (1 - R_{opt}^{AgNW}) \cdot T_{opt}^{AgNW}) \quad (12)$$

Unfortunately, both absorption and reflection coefficients of AgNW are not known experimentally and might differ significantly from bulk silver values. For instance, De *et al.*[29] obtained AgNW networks optical conductivity lower by more than one order of magnitude when compared with thin Ag film data. There is so far no clear explanation for such observations. However, the term within the outer set of brackets in Equation 12 can be assumed to be rather close to unity since T_{opt}^{AgNW} is lower than unity and the reflection coefficient of a AgNW is probably (like bulk Ag) close to unity. Therefore this is mainly the prefactor $\frac{4}{\pi \cdot d^{Ag} \cdot D_{NW}}$ which is supposed to dominate the β value. Accordingly, the slope values associated with large D_{NW} values (Ag117 and Ag138) are much smaller compared to small diameters (Ag26, Ag45 and Ag55). More quantitatively, the experimental slopes observed in Figure 6a span from 6.3.10^{-4} to 22.10^{-4} m^2.mg^{-1} while the calculated values of the prefactor (which corresponds to an over estimated value of the slope) are in the range from 8.8.10^{-4} to 47.10^{-4} for the AgNW diameters considered here. In spite of the model's simplicity, this shows a rather good agreement. Thus, it allows a fair comparison with experimental data explaining the linear dependence of the relative network transmittance versus areal mass density (Equation 11). These experimental values are close to those predicted by the model and the associated slope tendency is to increase in magnitude for small AgNW diameter.

It is often a problem to retrieve the exact value of transmittance for a layer which is supported by a substrate since in general interferences between the media have to be taken into account, as for the transparent conductive oxide layers. However, in the present case no clear interferences are present and a linear dependence of T_{opt} versus amd is observed, for this range of densities.
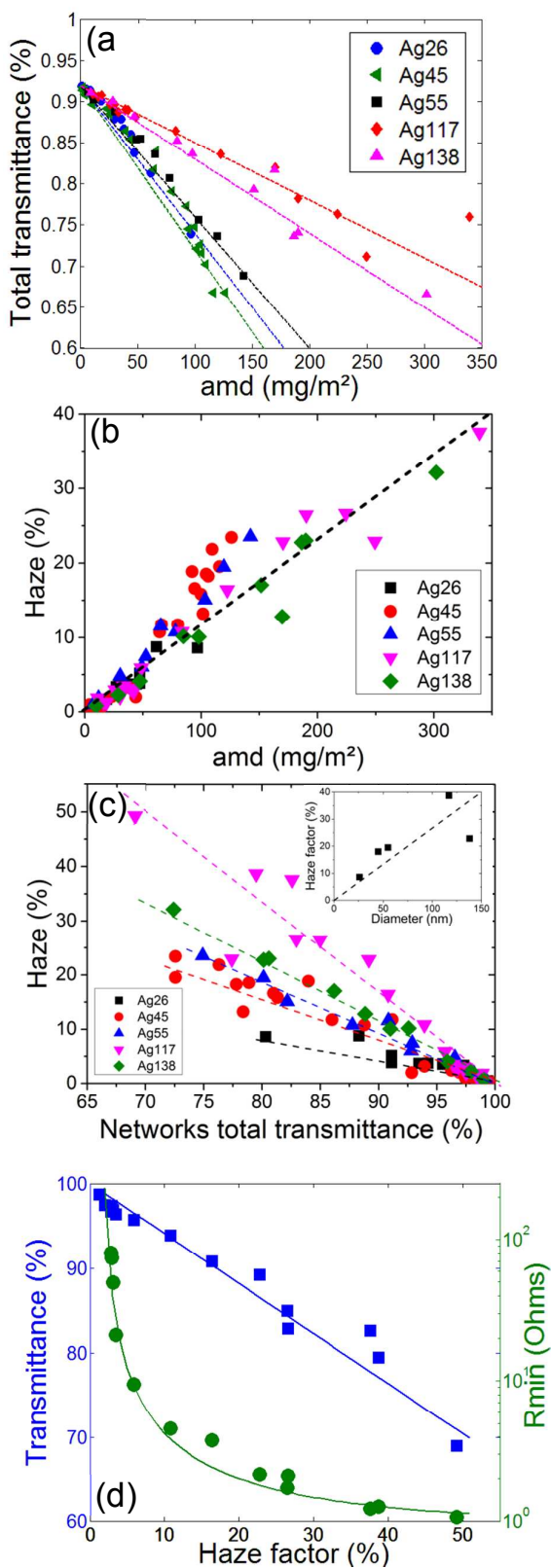
Figure 6: a) Experimental total transmittances values measured at λ=550 nm of AgNW networks of different areal mass densities and composed of different types of AgNWs

(markers). A linear fit of transmittance versus *amd* (dashed lines) is presented for each AgNW type, according to Equations 10a and 10b. b) Haze factor versus *amd* measured at λ=550 nm for samples made from nanowires with various dimensions and densities. The dashed line is a guide for the eyes showing the linearity of the haze factor versus *amd*. c) Experimental haze factor measured at λ=550 nm plotted versus optical transmittance showing a linear tendency, with a clear influence of the nanowire type. The insert shows the increase of the haze factor with AgNW diameter at a given optical transmittance (~80%) d) Minimum resistance and total transmittance at λ=550 nm of Ag117 networks with various densities versus the associated haze factor.

One can then, in a first approximation, suppose that the optical transmittance of the AgNW network can be obtained from T_{opt} divided by T_{opt}^0, the latter being the transmittance of the bare substrate. Under this hypothesis, except in Figure 6a, the transmittance data without substrate contribution are used in the next section to assess and compare transparent electrodes composed of AgNW of different morphologies.

Scattering of light is another important feature for a transparent electrode.[58] The haze factor is a parameter that quantifies the amount of light scattered by the material and is simply defined as the ratio between diffuse transmitted light and total transmitted light. The needs regarding transparent electrodes are different depending on applications. For example touch panels would need a low haze factor, high transparency and high conductivity,[62] while solar cells performance would be enhanced by a high haze factor,[63] but still need very high transmittances and conductivity. This is why investigations have been lately focused on fabricating transparent electrodes with enhanced haziness[64] since scattering light enhances the optical path length of photons in solar cells, increasing their probability of being absorbed.

The haze factor of all the samples studied is plotted in Figure 6b versus areal mass density. A linear trend is observed which is, in a first approximation, independent of the AgNW type. Figure 6b clearly shows that, independently of AgNW diameter, the haze factor appears to be directly proportional to the areal mass density. To get a better insight into the dependence of the networks haziness with nanowire dimensions, haze factor has been plotted in Figure 6c versus the network associated total transmittance T_{opt}. The haze factor is decreasing linearly with increasing T_{opt}, in agreement with Araki *et al.*[58] and Kim et *al.*[65] The different slopes observed in Figure 6c are, in first approximation, proportional to AgNW diameter, as shown in the insert. Physical modeling describing such observations is out of the scope of the present paper, however it shows that small diameters induce a decrease of the haziness in the visible spectrum owing to a lower efficiency of light scattering in this wavelength range.

Haze factor of AgNW networks has already been investigated in literature: for instance Araki *et al.*[58] showed that haze factor of AgNW networks can be decreased when using very long AgNW (20-100 µm), in agreement with Chang *et al.*[66] Preston *et al.*[59] observed experimentally that AgNW with higher diameters lead to higher haze factor in the visible range. Literature does not provide many detailed investigations which could explain these observed tendencies. Interestingly Khanarian *et al.*[62] reported an analysis of the optical properties of AgNW networks based on Mie light scattering theory. Such

approach enables to calculate both optical transmission and haze factor. These authors however used the surface area fraction covered by AgNW, instead of amd, as a key parameter. They obtained results in good agreement with the conclusions obtained here: AgNW diameter appears to be the morphological most important parameter that determines both transmission and haze.

Depending on dimensions and density, AgNW networks present a variability of electrical and optical properties. This is illustrated by Figure 6d where the minimum resistance as well as the transmittance of samples made of various densities of Ag117 networks are plotted against the haze factor. Similar trends were obtained by Araki *et al.*[58] Let us note that this figure can also be built for other types of nanowires as well, and can be seen as a guideline to find the optimum network density for a specific application.

2.7 Electrodes evaluation and comparison

To compare the performance of transparent electrodes in terms of density, a transmittance versus sheet resistance diagram is generally used.[29] In Figure 7a such a diagram is illustrated for samples of various densities made from Ag117. The sheet resistance was measured using the four point probe method after annealing for 2h at 200°C. This thermal process was shown in a previous study to optimize the electrical conductivity of samples with nanowires with similar dimensions.[35] The region of interest in Figure 7a is situated at low resistance and high transmittance, *i.e* top left region. The points were fitted using a combination of Equations 7 and 10b.

Another way to consider the performance of transparent conductive electrodes, and find the optimized density, is to calculate a figure of merit (FoM). For TCMs, and especially for solar cells applications, Haacke[45] proposed the following FoM for evaluating the balance between optical transparency and electrical resistance of thin films:

$$H = \frac{T^{10}}{R_s} \qquad (13)$$

Haackes figure of merit is generally calculated with transmittances T at 550 nm, which is standard for instance when solar cells applications are considered, and from the sample sheet resistance R_s. In this study, instead of R_s, we used the minimum 2 points resistance to calculate the Haackes FoM. This approximation was considered reasonable since at high network density, when the resistance is between 0 and 5 Ω, the data exhibits a linear dependence between R and R_s values. Typically, we could extrapolate R_s values from room temperature R_{min} by using the following equation:

$$R_s^{Extrap.} = \left(R_{min}^{RT} - R_0 \right) \cdot \frac{l}{d} \quad (14)$$

where R_0 is the instrumental resistance (0.8 Ω) and $\frac{l}{d}$ the ratio length/width of the studied electrodes.

The experimental sheet resistance measured by four point probe from Ag117 samples annealed at 200°C for 2h is plotted in Figure 7b against the extrapolated sheet resistance from the thermal ramp experiments that we just defined in Equation 14. The figure shows a clear agreement between calculated and experimental values. As the optimum density for each type of nanowires leads to resistances in the 0-10 Ω range (see Table 2), the use of 2 points resistance instead of sheet resistance is valid for the purpose of finding the best density of the different series.

To evaluate the influence of both density and AgNW dimensions, the Haacke FoM was calculated for all the investigated specimen of the present work. Among the five different wire types, samples made from Ag117 and Ag138 nanowires are the most promising as they exhibit the best optical and electrical properties. These samples FoMs are therefore plotted as an example against areal mass density in Figure 7c. A bell shape is observed, with the maximum FoM values indicating the range of optimum density, which can be fitted by using equations 7, 10b and 13. A good agreement is observed with rather scattered values for large areal mass density which arises from the uncertainty associated with the method used to determine amd experimentally, increasing for dense networks. It was then possible to extract the optimized density for each nanowire type. The characteristics (resistance, transmittance, amd and figure of merit) of each optimized sample have been displayed in Table 2. Seeking the optimized density shows that networks cannot all achieve the same FoMs, which depends on their morphology. In Figure 7c there is a clear dominance of Ag117 on Ag138 and therefore on the other nanowire types (such as Ag45 and Ag55, also represented in the figure).

A calculated optimum amd can be extracted from Figure 7c: a value close to 130 mg.m^{-2} for Ag117 and Ag138. Such amount of silver would correspond to a homogeneous layer of 12 nm thick, illustrating well the very low amount of silver used. If one uses directly the Pouillet's law, *i.e.* $R = \frac{\rho \cdot L}{S}$ for a layer of length

	Ag26	Ag45	Ag55	Ag117	Ag138
Best sample Rmin at 20°C (Ω) *	7.9	6.5	9.2	2.3	4.7
Best sample transmittance (%)	88.3	88.8	90.9	89.2	88.8
Best sample FoM (x10^{-3} Ω^{-1})	37	47	42	135	65
Best sample amd (mg.m^{-2})	62	64	65	170	170

Table 2: Experimental optical and electrical properties of optimized samples from the different nanowire type density series

* Note that the electrical resistances displayed in the table are two-points measured resistances and not sheet resistances (see section 2.7 for discussion).

L, section S and electrical resistivity ρ, the resulting electrical resistance R a layer 12 nm thick would then be equal to 0.8 Ω if the bulk silver value of ρ is considered. Added with the instrumental set-up resistance (R_0=0.8 Ω) the obtained value is very close to the observed R$_{min}$ for the Ag117 optimized sample in this study (2.3 Ω, see Table 2). This very simple calculation indeed shows that using a low amount of silver but in the shape

of NWs with diameter larger than the mean free path of the electrons instead of a thin layer, where surface scattering would have too large effects, constitutes a very efficient way to fabricate a transparent electrode.

Another way to compare networks made from different types of nanowires is shown in Figure 8a. It exhibits the FoM in an AgNW length-diameter phase diagram, plotted with a data disc size proportional to the maximum FoM value for the optimal density of each AgNW type studied here (red). Data from the literature (AgNW only) have also been plotted for comparison (green). This shows that the method proposed in this paper is an efficient way to optimize AgNW networks optical and electrical properties.
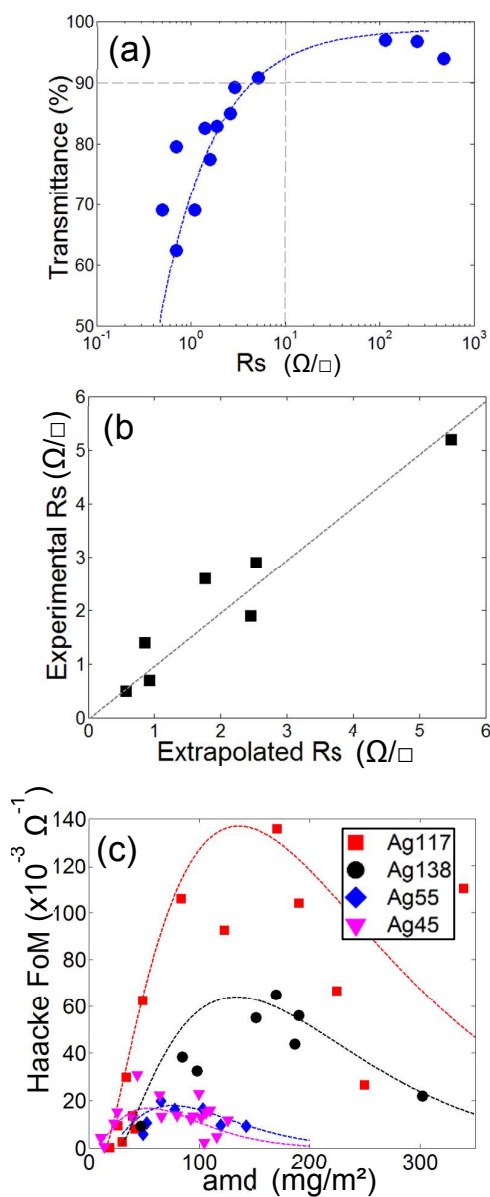

Figure 7: a) Transmittance values at 550 nm versus sheet resistance for Ag117 samples of various network densities. Sheet resistance was measured after a 200°C 2h annealing. The fit comes from equations 7 and 10b. b) Experimental sheet resistance measured by 4 point probe after a 200°C 2h annealing versus the extrapolated sheet resistance (Equation 14). Dashed line is a linear curve with a slope of 1 c) FoM against areal mass density of samples from Ag117, Ag138, Ag55 and Ag45 fitted by equation 7, 10a, 10b and 13.

Considering the nanowires studied here, network optical and electrical performances are enhanced in the large diameter/large length part of the graph. Especially, the largest length, Ag117, leads to a FoM much higher than the other nanowires. This is in good agreement with percolation equations and with the work of Bergin *et al.*[60] who showed experimentally that for nanowires with the same diameter, longer lengths led to better optical and electrical properties. While Figure 8a shows that longer and wider AgNW give rise to better FoM, very likely other parameters should also be taken into account. Among them, defects are also anticipated to play an important role. Such defects concern for instance grain boundaries along AgNWs which can lead to thermal grooving,[67] increasing the electrical resistance along with individual nanowires, and also decreasing the nanowires thermal and electrical stabilities. Furthermore, diameter and length distributions can influence the AgNW network behavior during thermal annealing. Therefore, while Figure 8a reveals a tendency that long and wide AgNWs are interesting for optimizing the FoM, this may also stem from possible lower values of defect density or length and diameter distributions which clearly depend on AgNW growth conditions. Based on the equations developed in this paper we would suggest that nanowires with diameters on the order of 100-120 nm with a length greater than 40 μm would produce excellent figures of merit.

Finally, for the sake of comparison with other transparent electrodes, Figure 8b shows the characteristics (T versus R_s) of different transparent conducting materials: ITO,[29,68] carbon nanotubes SW,[21,29,68] graphene,[15,16,68,69] copper[70–73] and silver nanowires[5,30,33,68,74] and FTO.[64] It can be seen that AgNW exhibit excellent properties comparable with ITO, if one considers the nanowires Ag117 investigated in the present work. This clearly shows that AgNW networks, if optimized in terms of network density, AgNW dimensions and thermal annealing, are an excellent material for transparent electrodes. This is of crucial importance for optimizing devices which depend on their electrodes electrical and optical properties such as solar cells or efficient transparent heaters. It is also worth noting that AgNW network are flexible and can be easily integrated into flexible devices, unlike most TCOs owing to their brittleness. However some other properties should be as well investigated, such as haze factor but also work function, stability (thermal, electrical, chemical) and roughness, which play an important role for integration in devices.
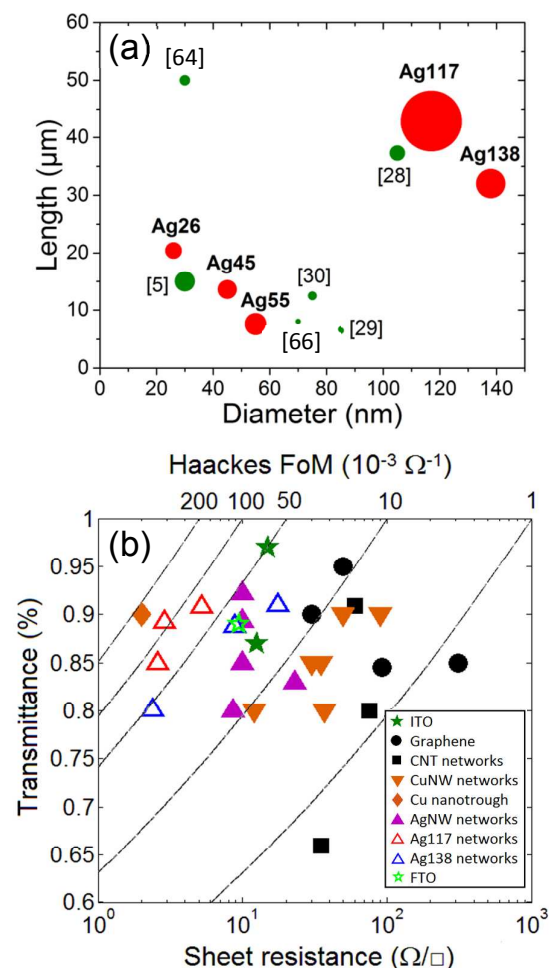
Figure 8: a) Figure of Merit from the best sample for each type of nanowire as a function of their length and diameter. Red markers are for the samples of the present study, and green marker for samples from the literature with reference inscribed into brackets[5,28–30,66,68]. The marker size is proportional to the FoM value. b) Transmittance versus sheet resistance diagram for comparison of various TCMs (recent literature results published after 2009): ITO,[29,68] Graphene,[15,16,68,69] Carbon nanotube networks,[21,29,68] Copper nanowires networks,[70–73] Copper nanotrough[75] Silver nanowires networks[5,30,33,68,74] as well as FTO[64] and best results in this study for Ag117 and Ag138. The dashed lines correspond to different iso-values of FoM: 200, 100, 50, 10, 1 with units $10^{-3}\,\Omega^{-1}$.

Conclusions

A thorough study has been performed on AgNW-based networks fabricated from nanowires with different dimensions (length and diameter); an optimum network density was found for each of them, leading to samples with high figure of merit thanks to thermal annealing.

In situ resistance measurements were performed to shed light on the network electrical behavior during thermal annealing and showed that interrupting the ramped thermal annealing at an optimum temperature enables one to reach a low electrical resistance in a reproducible way.

Simple models based on percolation theory and surface scattering were proposed, that linked the electrical resistance and optical transmittance of the networks to AgNW network density, nanowire length and diameter. Two original expressions were derived, one for the electrical resistance, the other for the optical transmittance. Both provide good agreement with the experimental observations, validating the models relating these physical properties to network density and AgNW morphology. These models include bulk material physical quantities, and could, in theory, be applied to metallic nanowires with different nature (gold or copper for instance).

Electrodes properties were compared by using the Haacke figure of merit. This work shows that an optimization approach is efficient for selecting nanowire morphology, network density and suitable thermal annealing in order to obtain transparent electrodes with excellent optical and electrical properties. Networks composed of Ag117 nanowires exhibit excellent results at the experimental optimum density, 170 mg.m^{-2}, with a transmittance T=89.2%, and an experimental sheet resistance of R_{sh}=2.9 $\Omega/\square$ (after a 200°C 2h annealing). These properties, coupled with a rather high haze factor (22.8 %) are highly beneficial for use as transparent electrodes in solar cells.

Compared to other transparent conductive materials, silver nanowires are shown to be very promising candidates as transparent electrodes and, apart from their excellent optical and electrical properties, they present many other advantages such as flexibility and low cost fabrication. This should be very helpful for replacing Indium Tin Oxide (ITO) in some applications and in flexible devices, in particular solar cells, displays, transparent heaters or radio frequency antennas.

Experimental section

Deposition was performed by spin coating a solution of AgNW dispersed in isopropanol on 2.5 cm by 2.5 cm Corning glass (C1737-S111) substrates. The nanowires were synthesized by Seashell Technology[76] by the polyol process.[77] Five types of AgNW with different characteristic dimensions, detailed in Table 1, were investigated. The samples were deposited from nanowire solutions of various concentrations but with a constant deposition volume of 1 ml. To achieve good surface coverage and minimize waste, we deposited the solution onto the rotating substrate (1500 rpm) in pulses (about 1 drops per second), and in two stages of 0.5 ml each with a 30 s pause between them, allowing the surface to dry. This results in more of the solution drying on the sample surface and hence a much denser coating than a similar one stage single injection approach.

The samples were characterized optically by a Perkin Elmer Lambda 950 UV-Visible-Near IR spectrophotometer equipped with an integrating sphere, allowing measurement of their total and direct optical transmittances. Measurements were performed on two different locations on each sample. The measurement spot area was 1.35 cm^2 for total transmittance measurements, and 0.44cm² for direct transmittance measurements. Averages for the direct and total transmittances were calculated for each sample, as well as the haze factor.

The initial 2.5 cm by 2.5 cm samples were then cut into four square parts. One was kept as a control sample and another for Scanning Electron Microscopy (SEM) imaging and density calculation. All SEM images were obtained on an environmental FEI Quanta 250 FEG SEM. The network density of each sample was calculated from 10 SEM images taken at different locations on each as deposited sample. The software Image J was used to calculate the areal fractional coverage which corresponds to the percentage of substrate surface covered by nanowires from which the areal mass density was deduced. Typically the ranges of densities that were studied were within 0.4 and 15-20 times the calculated critical density n_c. Higher densities were studied for Ag26 (up to 74 times n_c), and Ag117 (up to 36 times n_c). Two silver paint contacts in the form of strips were placed upon opposing edges of the third part of the sample which was then heated in air at a constant ramp rate of 2°C per minute from room temperature to 500°C while the resistance was measured *in situ* by using a two probes measurement setup using Keithley 2500 instruments. The size of the AgNW network electrode being measured was maintained constant with a 7 mm gap between the silver paint electrodes. The last quarter of the samples made from Ag117 were annealed at 200°C for 2h in order to reach their minimum resistance, and their sheet resistance was then measured with a four point probe Lucas Labo, pro4. About the other sample series Ag26, Ag45, Ag55 and Ag138, only resistances between two probes were measured, not the sheet resistance. The temperature coefficient of resistivity of the nanowires was calculated by measuring the resistance slope during cooling after a thermal ramp annealing stopped at the temperature of minimum resistance. This calculation was performed on samples made from various nanowire types (Ag117 and Ag45).

Acknowledgements

References

1   C. Celle, C. Mayousse, E. Moreau, H. Basti, A. Carella and J.-P. Simonato, *Nano Res.*, 2012, **5**, 427–433.
2   S. Sorel, D. Bellet and J. N. Coleman, *ACS Nano*, 2014, **8**, 4805–4814.
3   S. Ji, W. He, K. Wang, Y. Ran and C. Ye, *Small*, 2014, **10**, 4951–4960.
4   A. R. Madaria, A. Kumar and C. Zhou, *Nanotechnology*, 2011, **22**, 245201.
5   H. Lee, D. Lee, Y. Ahn, E.-W. Lee, L. S. Park and Y. Lee, *Nanoscale*, 2014, **6**, 8565–8570.
6   A. Kim, Y. Won, K. Woo, C.-H. Kim and J. Moon, *ACS Nano*, 2013, **7**, 1081–1091.
7   M. W. Rowell and M. D. McGehee, *Energy Environ. Sci.*, 2011, **4**, 131.
8   L. Song, A. C. Myers, J. J. Adams and Y. Zhu, *ACS Appl. Mater. Interfaces*, 2014, **6**, 4248–4253.
9   R. G. Gordon, *Mrs Bull.*, 2000, **25**, 52–57.
10 C. G. Granqvist, *Sol. En. Mat. & Solar Cells*, 2007, **91**, 1529–1598.
11 K. Ellmer, *Nat. Photonics*, 2012, **6**, 809–817.
12 A. Kumar and C. Zhou, *ACS Nano*, 2010, **4**, 11–14.
13 D. S. Hecht, L. Hu and G. Irvin, *Adv. Mater.*, 2011, **23**, 1482–1513.
14 P. Blake, P. D. Brimicombe, R. R. Nair, T. J. Booth, D. Jiang, F. Schedin, L. A. Ponomarenko, S. V. Morozov, H. F. Gleeson, E. W. Hill, A. K. Geim and K. S. Novoselov, *Nano Lett.*, 2008, **8**, 1704–1708.
15 U. Kim, J. Kang, C. Lee, H. Y. Kwon, S. Hwang, H. Moon, J. C. Koo, J.-D. Nam, B. H. Hong, J.-B. Choi and H. R. Choi, *Nanotechnology*, 2013, **24**, 145501.
16 S. Bae, H. Kim, Y. Lee, X. Xu, J.-S. Park, Y. Zheng, J. Balakrishnan, T. Lei, H. Ri Kim, Y. I. Song, Y.-J. Kim, K. S. Kim, B. Özyilmaz, J.-H. Ahn, B. H. Hong and S. Iijima, *Nat. Nanotechnol.*, 2010, **5**, 574–578.
17 J. van de Groep, P. Spinelli and A. Polman, *Nano Lett*, 2012, **12**, 3138–3144.
18 D. Hecht, L. Hu and G. Grüner, *Appl. Phys. Lett.*, 2006, **89**, 133112–133114.
19 P. N. Nirmalraj, P. E. Lyons, S. De, J. N. Coleman and J. J. Boland, *Nano Lett.*, 2009, **9**, 3890–3895.
20 E. M. Doherty, S. De, P. E. Lyons, A. Shmeliov, P. N. Nirmalraj, V. Scardaci, J. Joimel, W. J. Blau, J. J. Boland and J. N. Coleman, *Carbon*, 2009, **47**, 2466–2473.
21 D. S. Hecht, A. M. Heintz, R. Lee, L. Hu, B. Moore, C. Cucksey and S. Risser, *Nanotechnology*, 2011, **22**, 075201–075201–5.
22 B. S. Shim, J. Zhu, E. Jan, K. Critchley and N. A. Kotov, *ACS Nano*, 2010, **4**, 3725–3734.
23 A. R. Rathmell, S. M. Bergin, Y.-L. Hua, Z.-Y. Li and B. J. Wiley, *Adv. Mater.*, 2010, **22**, 3558–3563.
24 P. E. Lyons, S. De, J. Elias, M. Schamel, L. Philippe, A. T. Bellew, J. J. Boland and J. N. Coleman, *J. Phys. Chem. Lett.*, 2011, **2**, 3058–3062.
25 Y.-H. Ko, J.-W. Lee, W.-K. Choi and S.-R. Kim, *Chem. Lett.*, 2014, **43**, 1242–1244.
26 Y. S. Yun, D. H. Kim, B. Kim, H. H. Park and H.-J. Jin, *Synth. Met.*, 2012, **162**, 1364–1368.
27 D. Langley, G. Giusti, C. Mayousse, C. Celle, D. Bellet and J.-P. Simonato, *Nanotechnology*, 2013, **24**, 452001.
28 D. P. Langley, G. Giusti, M. Lagrange, R. Collins, C. Jiménez, Y. Bréchet and D. Bellet, *Sol. Energy Mater. Sol. Cells*, 2014, **125**, 318–324.
29 S. De, T. M. Higgins, P. E. Lyons, E. M. Doherty, P. N. Nirmalraj, W. J. Blau, J. J. Boland and J. N. Coleman, *ACS Nano*, 2009, **3**, 1767–1774.
30 A. Madaria, A. Kumar, F. Ishikawa and C. Zhou, *Nano Res.*, 2010, **3**, 564–573.
31 Y. Gao, P. Jiang, L. Song, L. Liu, X. Yan, Z. Zhou, D. Liu, J. Wang, H. Yuan, Z. Zhang, X. Zhao, X. Dou, W. Zhou, G. Wang and S. Xie, *J. Phys. Appl. Phys.*, 2005, **38**, 1061–1067.
32 Y. Sun, B. Mayers, T. Herricks and Y. Xia, *Nano Lett.*, 2003, **3**, 955–960.
33 T. Tokuno, M. Nogi, M. Karakawa, J. Jiu, T. T. Nge, Y. Aso and K. Suganuma, *Nano Res.*, 2011, **4**, 1215–1222.
34 J. Jiu, T. Sugahara, M. Nogi, S. Nagao and K. Suganuma, *13th IEEE Conference on Nanotechnology (IEEE-NANO)*, 2013, 15–18.
35 D. P. Langley, M. Lagrange, G. Giusti, C. Jiménez, Y. Bréchet, N. D. Nguyen and D. Bellet, *Nanoscale*, 2014, **6**, 13535–13543.

36 G. Guisti, D. P. Langley, M. Lagrange, R. Collins, C. Jiménez, Y. Bréchet and D. Bellet, *Int. J. Nanotechnol.*, 2014, **11**, 785–795.

37 J.-Y. Lee, S. T. Connor, Y. Cui and P. Peumans, *Nano Lett*, 2008, **8**, 689–692.

38 L. Hu, H. S. Kim, J.-Y. Lee, P. Peumans and Y. Cui, *ACS Nano*, 2010, **4**, 2955–2963.

39 S. B. Sepulveda-Mora and S. G. Cloutier, *J. Nanomater.*, 2012, **6**, 1–7.

40 S. De and J. N. Coleman, *MRS Bull.*, 2011, **36**, 774–781.

41 41S. De, P. J. King, P. E. Lyons, U. Khan and J. N. Coleman, *ACS Nano*, 2010, **4**, 7064–7072.

42 J. Li and S.-L. Zhang, *Phys. Rev. E*, 2009, **80**, 040104–040104–4.

43 M. Žeželj, I. Stanković and A. Belić, *Phys. Rev. E*, 2012, **85**, 021101–021106.

44 A. Aharony and D. Stauffer, *Introduction To Percolation Theory*, Taylor & Francis, London, 1991.

45 G. Haacke, *J. Appl. Phys.*, 1976, **47**, 4086–4089.

46 Y. Gao, P. Jiang, D. F. Liu, H. J. Yuan, X. Q. Yan, Z. P. Zhou, J. X. Wang, L. Song, L. F. Liu, W. Y. Zhou, G. Wang, C. Y. Wang, S. S. Xie, J. M. Zhang and D. Y. Shen, *J. Phys. Chem. B*, 2004, **108**, 12877–12881.

47 D.R. Lide, *CRC Handbook of chemistry and physics 2004-2005: A ready-reference book of chemical and physical data*, CRC press, Boca Raton, 2004.

48 A. Bid, A. Bora and A. K. Raychaudhuri, *Phys. Rev. B*, 2006, **74**, 035426–035426–8.

49 S. Karim, M. E. Toimil-Molares, A. G. Balogh, W. Ensinger, T. W. Cornelius, E. U. Khan and R. Neumann, *Nanotechnology*, 2006, **17**, 5954–5959.

50 E.K Drexler, *Nanosystems*, John Wiley & Sons, New York, 1988.

51 D. Vollath, *Nanomaterials: an introduction to synthesis, properties and applications*, Wiley-VCH Verlag GmbH & Co. KGaA, Weinheim, 2008.

52 G.L. Hornyak, H.F. Tibbals, J.Dutta, J.J. Moore, *Introduction to Nanoscience&Nanotechnology*, CRC press Taylor&Francis, Boca Raton, 2009.

53 K.K Nanda, A. Maisels, F.E. Kruis, H. Fissan and S.Stappert, *Phys. Rev. Lett.*, 2003, **91**, 106102.

54 W. Zhang, Y. Liu, R. Cao, Z. Li, Y. Zhang, Y. Tang and K. Fan, *J. Am. Chem. Soc.*, 2008, **130**, 15581–15588.

55 L. Klinger and E. Rabkin, *Acta Mater.*, 2006, **54**, 305–311.

56 A. Rytkönen, S. Valkealahti and M. Manninen, *J. Chem. Phys.*, 1997, **106**, 1888–1892.

57 D. Kondepudi, I. Prigogine, *Modern Thermodynamics: from heat engines to dissipative structures*, John Wiley & Sons Ltd, Chichester, 1988.

58 T. Araki, J. Jiu, M. Nogi, H. Koga, S. Nagao, T. Sugahara and K. Suganuma, *Nano Res.*, 2014, **7**, 236–245.

59 C. Preston, Y. Xu, X. Han, J. N. Munday and L. Hu, *Nano Res.*, 2013, **6**, 461–468.

60 S. M. Bergin, Y.-H. Chen, A. R. Rathmell, P. Charbonneau, Z.-Y. Li and B. J. Wiley, *Nanoscale*, 2012, **4**, 1996.

61 S. Zhu, Y. Gao, B. Hu, J. Li, J. Su, Z. Fan and J. Zhou, *Nanotechnology*, 2013, **24**, 335202.

62 G. Khanarian, J. Joo, X.-Q. Liu, P. Eastman, D. Werner, K. O'Connell and P. Trefonas, *J. Appl. Phys.*, 2013, **114**, 024302.

63 T. Chih-Hung, H. Sui-Ying, H. Tsung-Wei, T. Yu-Tang, C. Yan-Fang, Y. H. Jhang, L. Hsieh, W. Chung-Chih, C. Yen-Shan, C. Chieh-Wei and L. Chung-Chun, *Org. Electron.*, 2011, **12**, 2003–2011.

64 G. Giusti, V. Consonni, E. Puyoo and D. Bellet, *ACS Appl. Mater. Interfaces*, 2014, **6**, 14096–14107.

65 T. Kim, A. Canlier, G. H. Kim, J. Choi, M. Park and S. M. Han, *ACS Appl. Mater. Interfaces*, 2013, **5**, 788–794.

66 M.-H. Chang, H.-A. Cho, Y.-S. Kim, E.-J. Lee and J.-Y. Kim, *Nanoscale Res. Lett.*, 2014, **9**, 330.

67 W. W. Mullins, *J. Appl. Phys.*, 1957, **28**, 333.

68 T. M. Barnes, M. O. Reese, J. D. Bergeson, B. A. Larsen, J. L. Blackburn, M. C. Beard, J. Bult and J. van de Lagemaat, *Adv. Energy Mater.*, 2012, **2**, 353–360.

69 T. Sun, Z. L. Wang, Z. J. Shi, G. Z. Ran, W. J. Xu, Z. Y. Wang, Y. Z. Li, L. Dai and G. G. Qin, *Appl. Phys. Lett.*, 2010, **96**, 133301–133303.

70 A. R. Rathmell and B. J. Wiley, *Adv. Mater.*, 2011, **23**, 4798–4803.

71 S. Han, S. Hong, J. Ham, J. Yeo, J. Lee, B. Kang, P. Lee, J. Kwon, S. S. Lee, M.-Y. Yang and S. H. Ko, *Adv. Mater.*, 2014, **26**, 5808–5814.

72 L. Hu, H. Wu and Y. Cui, *MRS Bull.*, 2011, **36**, 760–765.

73 D. Zhang, R. Wang, M. Wen, D. Weng, X. Cui, J. Sun, H. Li and Y. Lu, *J. Am. Chem. Soc.*, 2012, **134**, 14283–14286.

74 D.-S. Leem, A. Edwards, M. Faist, J. Nelson, D. D. C. Bradley and J. C. de Mello, *Adv. Mater.*, 2011, **23**, 4371–4375.

75 H. Wu, D. Kong, Z. Ruan, P.-C. Hsu, S. Wang, Z. Yu, T. J. Carney, L. Hu, S. Fan and Y. Cui, *Nat. Nanotechnol.*, 2013, **8**, 421–425.

76 Seashell Technology website, **http://www.seashelltech.com/index.shtml,** (06 July 2013).

77 Y. Gao, P. Jiang, D. . Liu, H. . Yuan, X. . Yan, Z. . Zhou, J. . Wang, L. Song, L. . Liu, W. . Zhou, G. Wang, C. . Wang and S. . Xie, *Chem. Phys. Lett.*, 2003, **380**, 146–149.